Chapter 3

Recovering mixtures of OAM modes from randomness

In this chapter, we describe two different methods for the recovery of composition OAM modes of the helical beam from random light. The detailed theoretical basis, simulations, and experimental designs are discussed. The decomposition of retrieved OAM modes is also presented.

3.1 Introduction

Optical detection of an object with light has tremendous potential in non-destructive testing, characterization, in-situ quantitative measurement, etc. The facet of the object which is being examined depends on the facet of the light that is being measured. Information about the object and optical signal can be extracted from the light intensity profile or its phase structure in certain cases. Measurement of the intensity is easy in comparison to the measurement of the phase profile of the beam. Experimental measurement of the phase and complex field demands an interferometric method or multiple measurements. Information about an object's chemical composition can be interpreted by measuring light's wavelengths.

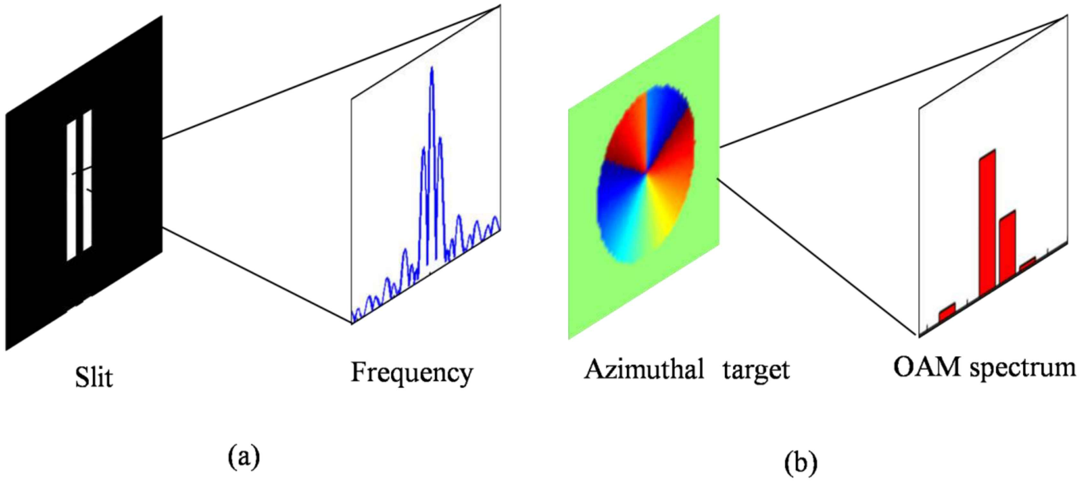

Fig. 3.1 (a) Slit and its spatial frequency, **(b)** Azimuthal target and its OAM spectrum.

Similarly, an object's spatial feature and topology can be analyzed by the composition of spatial frequency contents of the light. Such spatial frequency compositions help to understand, and examine propagation-induced effects in the light signal and also examine fine features of the object. The content and strength of the spatial frequency component $(p)$are connected with the position vector $\hat{r}$. Linear momentum (p) and position $\hat{r}$ are both unbounded and continuous variables of a physical system and are related by a continuous Fourier transform (Yao, 2006). On the other hand, angular structure $\Psi(\varphi)$ and OAM spectrum (l) are related by a Fourier series leading to discrete values of the angular momentum. Considering a Fourier relationship between the distribution of OAM spectra and the angular structure $\Psi(\varphi)$, we can connect one variable with another (Yao, 2006; Xie, 2017; Milione, 2017) as

$$\Psi(r,\varphi) = \frac{1}{\sqrt{2\pi}}\sum_{l=+\infty}^{l=+\infty} C_l\,(\mathrm{r})\exp(il\varphi)$$

where $C_l(r)$ are complex coefficients and the summation is over all (l). Tailoring in the angular distribution of the light or the object appears in the OAM spectrum. Therefore, evaluation of the OAM spectrum is important to understand the optical signal for a wide range of applications starting from communication to metrology.

Several techniques have been proposed over the years to detect OAM mode compositions. These techniques include mode decomposition using digital hologram (Litvin, 2012; Schulze, 2013), probing the OAM spectrum using the tilted lens (Miyamoto, 2019), analysis of the OAM spectrum using the holographic approach, and spatial light modulator (Pinnell, 2020), measuring the OAM spectrum by digital analysis of interference pattern (D'Errico, 2017). In addition, the OAM discrimination method was developed to measure FOV and identify the difference between intrinsic OAM and total OAM for fractional OAM states (Berger, 2018). A method was proposed to quantitatively measure non-integer OAM with a cylindrical lens and a camera (Alperin, 2016). Recently, a method was proposed for the precision measurement of fractional OAM based on a two-dimensional multifocal array consisting of different integer vortices (Deng, 2019). The OAM sorting methods based on the ray optics coordinate transformation have also been developed (Hossack, 1987; Wen, 2018). A computational method is also demonstrated for high-resolution recognition of FOV using machine learning (Liu, 2019). However, these methods consider propagation in free space or homogeneous media.

Significantly, the propagation of coherent light through disordered scattering media is a common issue in communication, imaging, etc. Propagation of the beam through scattering media influences the OAM spectrum and possibly leads to cross-talks between different OAM modes (Gong, 2019). This limits their use in practical applications such as remote sensing, optical communication, and imaging (Chen, 2014; Willner, 2021). Propagation of an optical beam in the presence of scattering media such as atmospheric turbulence, foggy medium, rain, and underwater affects the beam performance owing to scrambling in space and time. The inhomogeneity in the optical path lengths of the scattering media inevitably distorts the incident wavefront of the coherent light and generates a speckle pattern (Goodman, 2007))). These speckle patterns do not have any direct resemblance with the incident beam or OAM composition. Therefore, the direct detection of the OAM composition with the aforementioned conventional techniques is not possible in the presence of scattering media and hence limits the execution of these techniques (Alperin, 2016; Berger, 2018; Deng, 2019; D'Errico, 2017; Hossack, 1987; Litvin, 2012; Liu, 2019; Miyamoto, 2019; Pinnell, 2020; Schulze, 2013; Wen, 2018). Moreover, the previously mentioned techniques are not capable to measure the OAM spectrum of the obscured beam. Some significant techniques have been developed in the last decade to recover the coherent optical signal in the presence of the diffuser by utilizing the information-bearing features of the speckle patterns (Chen, 20211; Salla, 2015; Vinu, 2016). In addition, some researchers have analyzed the cross-covariance of the partially coherent beam, and some detection techniques were proposed to restore the partially coherent light (Ding, 2014; Lu, 2019; Singh, R., 2015). Additionally, incoherent light has also been utilized to discriminate the incoherent vortex and in the sorting of incoherent vortex modes (Bezerra, 2020; Huang, 2021; Liu, 2019).

3.2 Higher-order polarization correlation

Consider a transversely polarized beam with orthogonal polarization states x and y coaxially propagates through a random scattering medium and further travels down to the observation plane located in the far field. The random scattering leads to a speckle pattern at the observation plane and the complex field of the scattered light is represented as.

$$E(r) = \hat{e}_x E_x(r) + \hat{e}_y E_y(r), \tag{3.1}$$

where $E(r)$ indicates the scattered light at the far field and r represents the spatial position vector at the observation plane. The fluctuations between the SPs of the random field provide the complex polarization correlation function which carries the information of the target beam. The SPs can be expressed in terms of four Pauli spin matrices (Kuebel, 2019) as

$$S_n(r) = E^{\dagger}(r)\sigma^n E(r), \qquad (n=0,\ 1,\ 2,\ 3), \tag{3.2}$$

where † represents the Hermitian conjugate, σ^0 is the 2-by-2 identity matrix and $\sigma^1, \sigma^2, \sigma^3$ are the 2-by-2 three Pauli spin matrices, and

$$E(r) = \begin{pmatrix} E_x(r) \\ E_y(r) \end{pmatrix}. \tag{3.3}$$

Hence,

$$S_n(r) = \sum_{a,b} \sigma^n_{ab} E^*_a(r) E_b(r), (a,b = x, y). \tag{3.4}$$

The fluctuations of each SP around their average value can be defined as

$$\Delta S_n(r) = S_n(r) - < S_n(r) >, (n=0,\ 1,\ 2,\ 3) \tag{3.5}$$

where $S_n\left(r\right)$ is the SP pertaining to a single realization of the field at a specific spatial point and $< S_n(r) >$ denotes its ensemble average. The 4 x 4 matrix $C_{nm}\left(r_1, r_2\right)$ of SPs correlations can be defined (Wu, 2019) as follows:

$$C_{nm}(r_1, r_2) =< \Delta S_n(r_1) \Delta S_m(r_2) >, (n,m=0,1,2,3,) \tag{3.6}$$

Using the Gaussian moment theorem, the 4 x 4 Stokes fluctuations correlations matrix is transformed as

$$C_{nm}(r_1, r_2) = \sum_{a,b} \sum_{c,d} \sigma^n_{ab} \sigma^m_{cd} W_{ad}(r_1, r_2) W^*_{bc}(r_1, r_2), \tag{3.7}$$

The elements of the 4 x 4 complex polarization correlation matrix are evaluated from Eq. (3.7) and these elements are defined as

$$\begin{pmatrix} C_{00}(r_1,r_2) & C_{01}(r_1,r_2) & C_{02}(r_1,r_2) & C_{03}(r_1,r_2) \\ C_{10}(r_1,r_2) & C_{11}(r_1,r_2) & C_{12}(r_1,r_2) & C_{13}(r_1,r_2) \\ C_{20}(r_1,r_2) & C_{21}(r_1,r_2) & C_{22}(r_1,r_2) & C_{23}(r_1,r_2) \\ C_{30}(r_1,r_2) & C_{31}(r_1,r_2) & C_{32}(r_1,r_2) & C_{33}(r_1,r_2) \end{pmatrix}. \tag{3.8}$$

3.3 Recovering a mixture of OAM modes and fractional charge from randomness

In order to demonstrate the use of higher-order Stokes Parameters (SPs) fluctuation correlations in the recovery of the composition of the OAM modes from the randomness, we considered an optical beam which fractional topological charges. These beams with fractional topological charges are made of contributions from the OAM spectrum (Deng, 2019). Out of the sixteen elements of the Stokes parameters correlation matrix, we use only four elements help to extract the complex polarization correlation function (CPCF) from spatially fluctuating random light. Hereinafter, the complex field from the CPCF projection over the helical basis is applied to examine the composition of the OAM spectrum and determine the weightage of the spectrum. Our technique is free from using the specialized mask and additionally non-interferometric, iteration-free, and free from the pre-calibration requirement of the scattering medium (Gong, 2019). Due to these unique features, our experimental method offers high flexibility and robustness. The proposed theoretical framework is verified by simulation results and also confirmed by experimental results. The application of our technique is demonstrated in the recovery of the quantitative information of the fractional optical vortex (FOV) obscured by the random scattering medium and measuring the decomposition of the FOV in different integer OAM states. The detailed theoretical explanation, simulation results, and the corresponding experimental test are discussed below.

3.3.1 Theory

Now the elements $C_{20}(r_1,r_2), C_{21}(r_1,r_2), C_{30}(r_1,r_2)$, and $C_{31}(r_1,r_2)$ of the polarization correlation matrix represented in Eq. (3.8) are explored to develop a detection technique for the object obscured by a random scattering medium and consequently, recover the compositions of OAM modes from random light. The real part of the CPCF is obtained by adding the elements $C_{20}(r_1,r_2)$ and $C_{21}(r_1,r_2)$. Similarly, the imaginary part of the CPCF is evaluated by adding the elements $C_{30}(r_1,r_2)$ and $C_{31}(r_1,r_2)$. Finally, the CPCF is calculated by adding real and imaginary parts as follows

$$C(r_1,r_2) = (C_{20}(r_1,r_2) + C_{21}(r_1,r_2)) + i(C_{30}(r_1,r_2) + C_{31}(r_1,r_2))$$

$$C(r_1,r_2) = C_{\mathrm{Re}}(r_1,r_2) + iC_{\mathrm{Im}}(r_1,r_2)$$

$$C(r_1,r_2) = 4\,\mathrm{Re}[W_{xx}(r_1,r_2)W^{*}_{yx}(r_1,r_2)] + i4\,\mathrm{Im}[W_{xx}(r_1,r_2)W^{*}_{yx}(r_1,r_2)], \tag{3.9}$$

where $W_{ab}(r_1, r_2) = \left\langle E_a^*(r_1) E_b(r_2) \right\rangle$, (a, b=x, y), represents the elements of the 2-by-2 coherence polarization (CP) matrix which analyze the statistical properties of the random light.

Let us examine the use of Eq. (3.8) for the recovery of an optical signal which is a composition of OAM modes. Here, the target signal i.e composition of helical beams $A_0(\hat{r})\exp(i\psi)$ are loaded into the x-polarized component and the y-polarized component is a plane wave. Here, $A_0(\hat{r})$, A represent the amplitude of the target beam and plane wave respectively. ψ indicates the phase structure of the target beam and $\hat{r}$ is the spatial position vector at the source plane. *A* complex field represented in Eq. (3.1) and is connected to the source plane as depicted in Fig. 3.2 as

$$E(r) = \int E(\hat{r}) \exp\left[i\delta(\hat{r})\right] \exp\left[-i\frac{2\pi}{\lambda f} r.\hat{r}\right] d\hat{r}, \tag{3.10}$$

where $E(\hat{r}) = A_0(\hat{r})\exp(i\psi)\hat{e}_x + A\hat{e}_y$. $\delta(\hat{r})$ is the random phase introduced by the random scattering layer, *f* is the focal length of the Fourier transforming lens, and λ is the wavelength of the incident light. Substituting Eq. (3.10) into Eq. (3.9) helps to connect the CPCF with the elements of the CP matrix as follows

$$W_{ab}(r_1, r_2) = \left\langle \int\int\int E_a^*(\hat{r}_1) E_b(\hat{r}_2) \exp\left[-i(\delta(\hat{r}_1) - \delta(\hat{r}_2)\right] \times \exp\left[-i\frac{2\pi}{\lambda f}(r_2.\hat{r}_2 - r_1.\hat{r}_1) d\hat{r}_1 d\hat{r}_2\right] dr_1 \right\rangle, \tag{3.11}$$

where <.> represents the ensemble average. A space average is taken into account on the assumption of spatial stationarity and ergodicity, and $\Delta r = r_2 - r_1$. Therefore, Eq. (3.11) at the Fourier transform plane modifies to

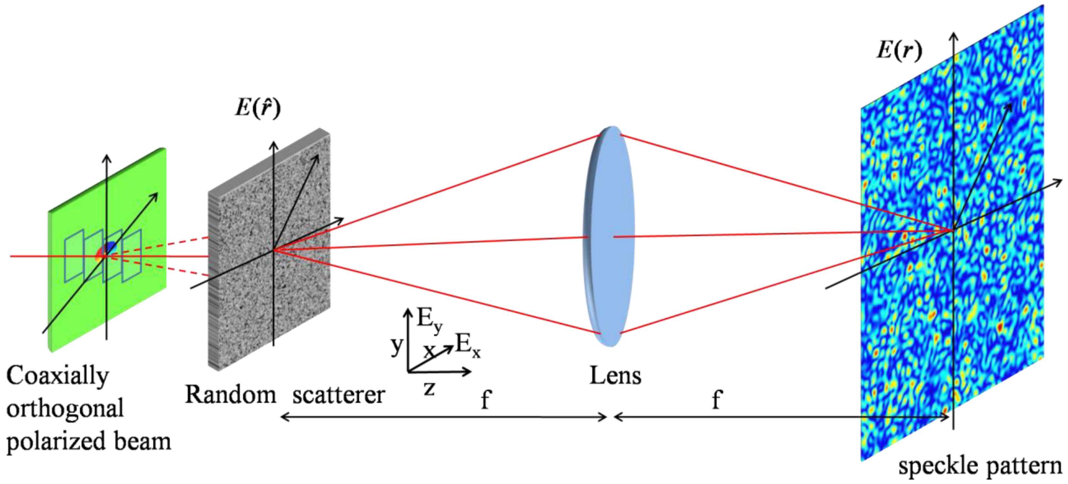

Fig. 3.2 Schematic representation of f - f geometry and the formation of speckle at the Fourier transform plane.

$$W_{ab}(\Delta r) = \int \left\{ \int\int E_a^*(\hat{r}_1) E_b(\hat{r}_2) \exp\left[-i(\delta(\hat{r}_1) - \delta(\hat{r}_2)\right] \times \exp\left[-i\frac{2\pi}{\lambda f}((r_1 + \Delta r).\hat{r}_2 - r_1.\hat{r}_1) d\hat{r}_1 d\hat{r}_2 \right] \right\} dr_1, \tag{3.12}$$

Taking into account of the delta function resulting from the spatial averaging at the observation plane due to $\int \exp\left(-\frac{ik}{f}(\hat{r}_2 - \hat{r}_1).r_1 \right) dr_1 = \delta(\hat{r}_2 - \hat{r}_1)$, Eq. (3.12) modifies to

$$W_{ab}(\Delta r) = \int E_a^*(\hat{r}_1) E_b(\hat{r}_1) \exp\left(-\frac{ik\Delta r.\hat{r}_1}{f} \right) d\hat{r}_1, \tag{3.13}$$

Eq. (3.13) states that the polarization correlation at the observation plane is the Fourier transform of the polarized source at the diffuser plane. This equation is nothing but the vectorial vCZ connected vectorial coherence at the far field with the incoherent/random polarized source (Singh, R., 2013). The spatial stationarity at the observation plane was achieved by removing the non-stationarity phase factor using a Fourier transforming lens of focal length f (Takeda, 2014) as shown in Fig. 3.2.

Therefore,

$$W_{xx}(\Delta r)W_{yx}^{*}(\Delta r)=\int E_x^{*}(\hat{r}_1)E_x(\hat{r}_1)\exp\left(-\frac{ik\Delta r.\hat{r}_1}{f}\right)d\hat{r}_1\left\{\int E_y^{*}(\hat{r}_1)E_x(\hat{r}_1)\exp\left(-\frac{ik\Delta r.\hat{r}_1}{f}\right)d\hat{r}_1\right\}^{*}$$

(3.14)

where $E_x(\hat{r}_1)=A_0(\hat{r})\exp(i\psi)$, and $E_y(\hat{r}_1)=A.$ Equation (3.9) states that the complex amplitude of the un-known optical beam can be recovered from the speckle pattern. In order to utilize Eq. (3.9) in the OAM mode analysis, a background coherence function $W_{xx}(\Delta r)$ is considered to provide a constant cover over the desired complex coherence $W_{yx}^{*}(\Delta r)$. The recovered complex field can be decomposed to examine the OAM states of the incident object beam.

To demonstrate the application of the proposed technique in the measurement of the OAM spectrum, we considered the FOV as an object that is obscured by a random scattering medium. For fractional values of l the phase factor $\exp(i\psi)$ in Eq. (3.1) can be represented as $\exp(il\varphi)$, where $\psi = l\varphi$ and characterized in terms of a superposition of all the integer OAM modes as (Deng, 2019).

$$\psi=\sum_{n=-\infty}^{\infty}C_n(l)\exp(in\varphi). \tag{3.15}$$

where C_n can be represented as

$$C_n(l)=\frac{\exp(il\pi)\sin(l\pi)}{\pi(l-n)},$$

where $l=n+\varepsilon$, n is an integer number and ε is a small fraction. Therefore, the light beam with fractional OAM modes could be deemed as multiplexing integer OAM beams with different weights.

3.3.2 Simulation results

In order to quantitatively compare the performance of our technique and compare results of the phase reconstruction of the FOV obscured by a random scattering medium, we have simulated a free space propagation of the FOV at the far field. The free-space propagation in a far field is considered for a complex field represented as $A_0(\hat{r})\exp(il\varphi)$, where l is a fractional topological charge. A far-field propagation is realized by using the standard fast Fourier transform for a complex field represented at source $z=0$ plane with initial phase-shift, and the results are shown in Fig. 3.3. Simulated free space propagation results of the amplitude and phase distribution of the FOV with $l=-0.5$, 0.5, and 1.5 are shown in Fig. 3.3. Figs. 3.3, (a-c) represent amplitude distribution, and 3.3, (d-f) are the corresponding phase distribution. A similar Fourier transform relation also exists between the Fourier spectrum and the FOV structure at the random scattering medium as represented by Eq. (3.16) under consideration of the spatial stationarity and ergodicity in our given geometry as shown in Fig. 3.3. Condition of spatial stationarity and spatial averaging at the detector plane provides a connection between the polarized random source structure and coherence in the far-field as given in Eq. (3.10) and this Eq. represents the vCZ. The vectorial vCZ theorem used in our work is derived under consideration of ergodicity in space (rather than in time) and taking the space average over the observation plane (rather than over the source plane). This equation is very similar to the free space Fourier relation connecting the source with its far field. Therefore, a far-field pattern of the FOV in the free space can be compared with the CPCF result for the FOV through a random scattering media. The simulation results of the propagation of polarized light through a random scattering medium are shown in Fig. 3.4 for three non-integer TC values with $l=-0.5$, 0.5, *and* 1.5. The random scattering medium is modeled as a phase screen under the condition of uniformly distributed random phasors in the interval $[-\pi,\pi]$.

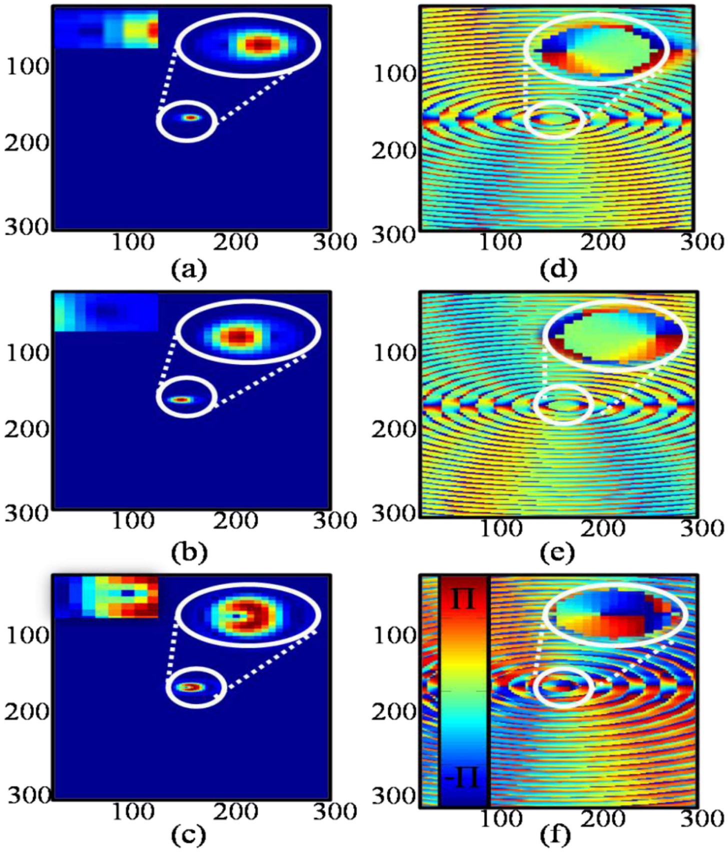

Fig. 3.3 Simulation results for free space; **(a-c)** represent amplitude distribution for three different cases *l=-0.5, 0.5, 1.5,* **(d-f)** are the corresponding phase distribution. The dark lines in the amplitude distribution are highlighted in the inset.

The random phase screen generates a fully developed speckle that follows Gaussian statistics (Goodman, 2005, 2007). Simulation results of the amplitude and phase distribution of the CPCF for a given situation of the incident FOV with *l=-0.5, 0.5,* and *1.5* are shown in Fig. 3.4. The results in Figs. 3.4, (a-c) show amplitude distribution, and (d-f) show phase distribution of CPCF for *l=-0.5, 0.5,* and *1.5.* Figs. 3.4, (a-c) reveal a dark line in the amplitude distribution of the CPCF. The OAM mode in one of the orthogonal polarization components of incoming light forms a dark line in the amplitude distribution of the CPCF. The quality of reconstruction is also assessed by comparing results in Fig. 3.4 with results in Fig. 3.3 for free-space propagation, and a good agreement is found between the two. To quantitatively investigate the different integer OAM modes of FOV with *l=-0.5, 0.5, 1.5,* the spatial phase structures of the CPCF are shown in Figs. 3.4, (d-f). The spatial phase distribution of CPCF in Figs. 3.4, (d-f) reveal the phase profile of FOV.

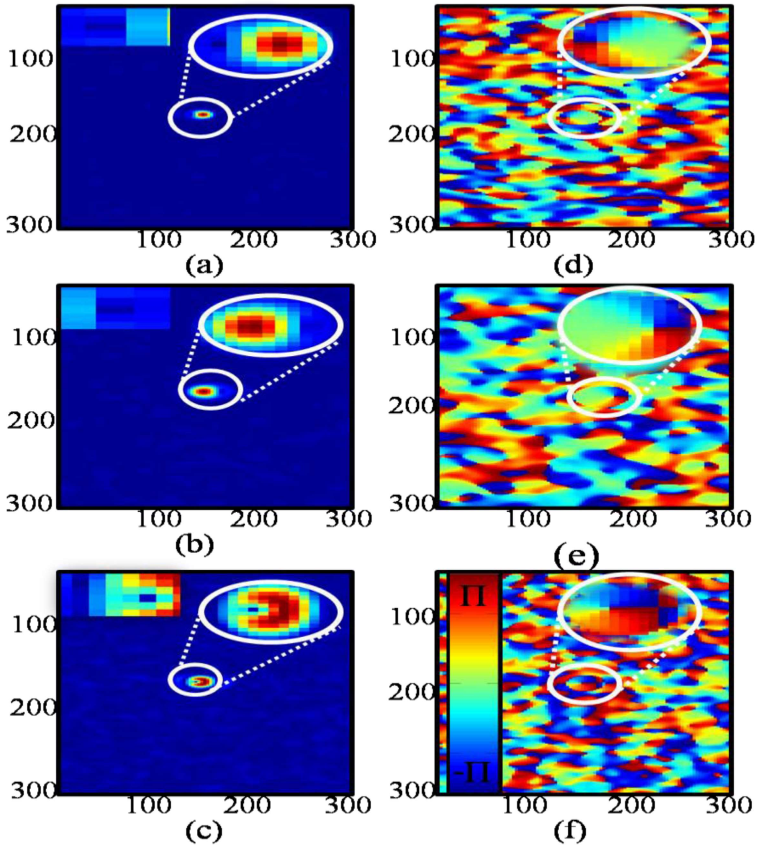

Fig. 3.4 Simulation results for random media; **(a-c)** represent amplitude distribution of CPCF for three different cases *l=-0.5, 0.5, 1.5,* **(d-f)** are the corresponding phase distribution. The dark lines in the amplitude distribution are highlighted in the inset.

3.3.3 Experiment and results discussions

The proposed experimental setup for measuring the OAM spectrum is shown in Fig. 3.5. A spatially filtered He-Ne laser light beam of wavelength 633 nm is attenuated with a neutral density filter (NDF) which reduces the unwanted power of the beam. The half-wave plate (HWP) is used to orient the incoming beam at 45^0 with respect to the horizontal direction. The 50:50 beam splitter divides the 45^0 polarized beams into two equal-intensity beams. The beam transmitted from BS is used to illuminate a phase-only spatial light modulator (SLM) with a resolution of 1920 x 1080 and a pixel pitch of 8 μm (Pluto from Holoeye) working in the reflection mode. The SLM is used to load the FOV phase structure. This SLM modulates only the x-polarization component which is loaded with the FOV and the y-polarization component remains intact i.e. plane wave.

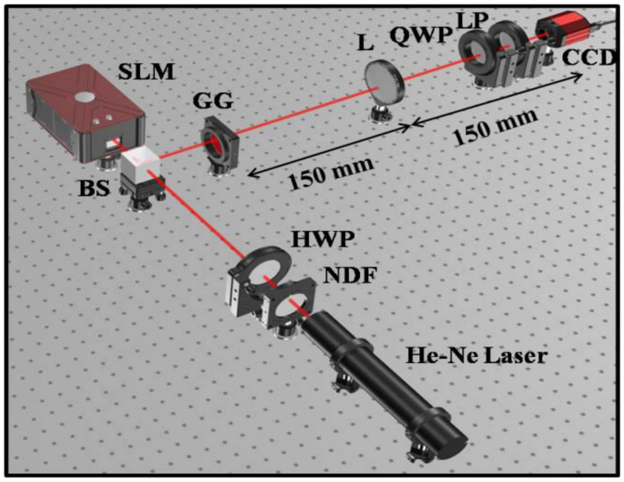

Fig. 3.5 Sketch of the experimental set-up of the proposed technique. He-Ne Laser, NDF: Neutral density filter, HWP: Half-Wave plate, BS: Beam splitter, SLM: Spatial light modulator, GG: Ground glass, L: Lens, QWP: Quarter-Wave plate, LP: Linear polarizer, CCD: Charge-coupled device.

The reflected beam from SLM is directed towards a diffuser by a reflection from BS. The diffuser is a ground glass (GG) from Thorlab [Model No. DG 10-600-MD]. Further, the beam propagates through the GG and is randomly scattered, the GG scrambles the incident light and generates a speckle pattern. The random field from the GG is Fourier transformed by a lens (L) of focal length 150 mm as described by Eq. (3.2).

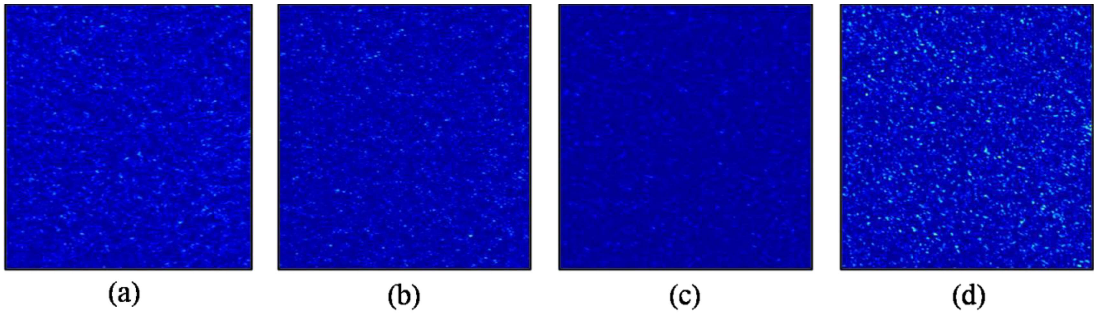

Fig. 3.6 Represents experimentally measured SPs *(a)* S_0 *(b)* S_1 *(c)* S_2 *and (d)* S_3.

The polarization states of the speckle pattern are characterized in a highly stable non-interferometric set-up by measuring the SPs using a quarter-wave plate (QWP) and linear polarizer (LP) combination as shown in Fig. 3.5. The different combinations of QWP and LP are used to record the intensity distribution of the speckle using a charge-coupled device (CCD) camera with a dynamic range of 8-bit and resolution of 1280 x 1024 pixels and a pixel pitch of 4.65 μm [Thorlab Model No. DCU224M]. The CCD captures the intensity pattern and the four SPs are determined from the captured speckle patterns by using the following equations (Brundavanam, 2012).

$$\begin{aligned} S_0(r) &= I(0^0,0^0)+I(90^0,90^0), \\ S_1(r) &= I(0^0,0^0)-I(90^0,90^0), \\ S_2(r) &= I(45^0,45^0)-I(135^0,135^0), \\ S_3(r) &= I(0^0,45^0)-I(0^0,135^0), \end{aligned} \tag{3.16}$$

where$I(\theta_q,\theta_p)$ is the intensity at the observation plane when the axes of the QWP and LP are at θ_q and θ_p respectively as measured from the horizontal direction. The experimentally measured SPs shown in Fig 3.6 is used to evaluate the correlations of the fluctuations of the SPs. Further, the experimentally measured SPs help to evaluate the real and imaginary parts of the two-point CPCF using Eq. (3.9). The CPCF between two orthogonal polarization components is evaluated using Eq. (3.14). The speckle pattern in Fig. 3.6, (a-d) show experimentally measured four SPs S_0, S_1, S_2, and S_3 from captured intensity pattern by the CCD. The speckle grain size in Fig. 3.6 depends on the polarized aperture, wavelength, and observation distance as described in Eq. (3.13). Experimental results of the amplitude and phase distribution of the incident FOV located behind the diffuser with *l=-0.5, 0.5,* and *1.5* are shown in Fig. 3.7. Figs. 3.7, (a-c) show amplitude distribution, and (d-f) show phase distribution.

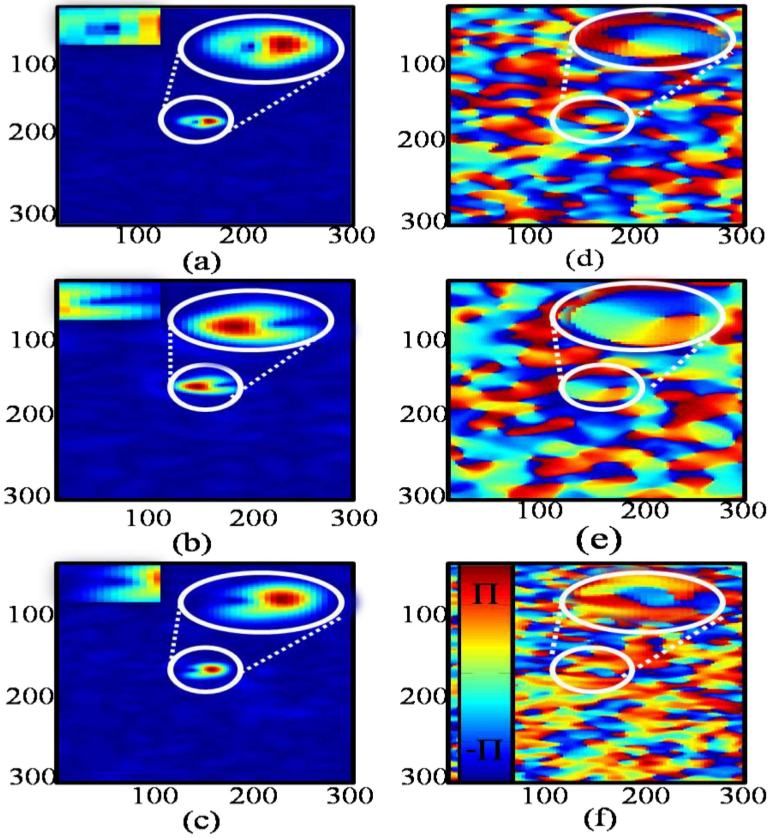

Fig. 3.7 Experiment results for random media; **(a-c)** represent amplitude distribution of CPCF for three different cases *l=-0.5, 0.5, 1.5,* **(d-f)** are the corresponding phase distribution. The dark lines in the amplitude distribution are highlighted in the inset.

These experimentally recovered phase structures for the incident FOV are also compared with simulation results as shown in Fig. 3.4 and good agreement is found between the two.

3.3.4 OAM modes decomposition and their need

The high data rates in optical communication have been achieved using several multiplexing schemes such as wavelength division multiplexing (WDM), polarization division multiplexing (PDM), mode division multiplexing (MDM), and so on (Willner, 2015). The OAM modes with various l are theoretically infinite and orthogonal to one another in Hilbert space which forms a suitable basis set of nonoverlapping channels for MDH. In MDH, the different spatial modes are used as information-carrying channels and co-axially propagated through the scattering media. The presence of scattering media in the propagation channel scrambles these spatial modes and leaks one mode into another mode. In such cases, the receiver at the observation plane detects the superposition of OAM modes and it is significant to sort and quantify the model weight of the numerous modes present in the resultant beam. The sorting of OAM modes is referred to as modal decomposition and shows the potential application in wavefront reconstruction, beam quality measurements, etc.

In the proposed technique, experimental geometry in Fig. 3.5 helps to retrieve the CPCF from a non-interferometric set-up and this complex quantity is used to evaluate the OAM spectrum. We use the orthogonal projection method to decompose the different integer OAM modes in terms of the OAM power spectrum. To decompose the different integer OAM modes of the target FOV, an experimentally measured far-field spectrum of FOV is projected onto spiral harmonics $e^{in\varphi,}$ where n is the integer topological charge. The complex coefficient A_n is evaluated by integrating the recovered far-field FOV with respect to the azimuthal angle. The complex coefficient C_n carries each OAM value as a function of the radial coordinates. Now, the OAM power spectrum of the beam is investigated by integrating the modulus square of C_n. Further, the OAM power spectrum is used to represent each OAM component in terms of azimuthal modes (Molina-Terriza, 2001).

The angular Fourier transform is applied over the recovered far-field FOV to evaluate the complex coefficient $C_n(\Delta r)$.

$$C_n(\Delta r) = \frac{1}{2\pi}\int_0^{2\pi} d\varphi e^{-in\varphi}\, C(\Delta r). \tag{3.17}$$

The complex coefficient is used to investigate the OAM power spectrum of the FOV beam by integrating $|C_n(\Delta r)|^2$ it with the radial coordinates.

$$P(n) = \frac{1}{S}\int_0^{\infty} drr|C_n(\Delta r)|^2. \tag{3.18}$$

where,$S = \sum \int_0^{\infty} drr|C_n(\Delta r)\,|^2$denotes beam power and $P(n)$ denotes the OAM power spectrum. A retrieved CPCF result is substituted in Eq. (3.17) and (3.18) to evaluate the OAM spectrum of the FOV obscured by the scattering medium for experimental and simulated cases.

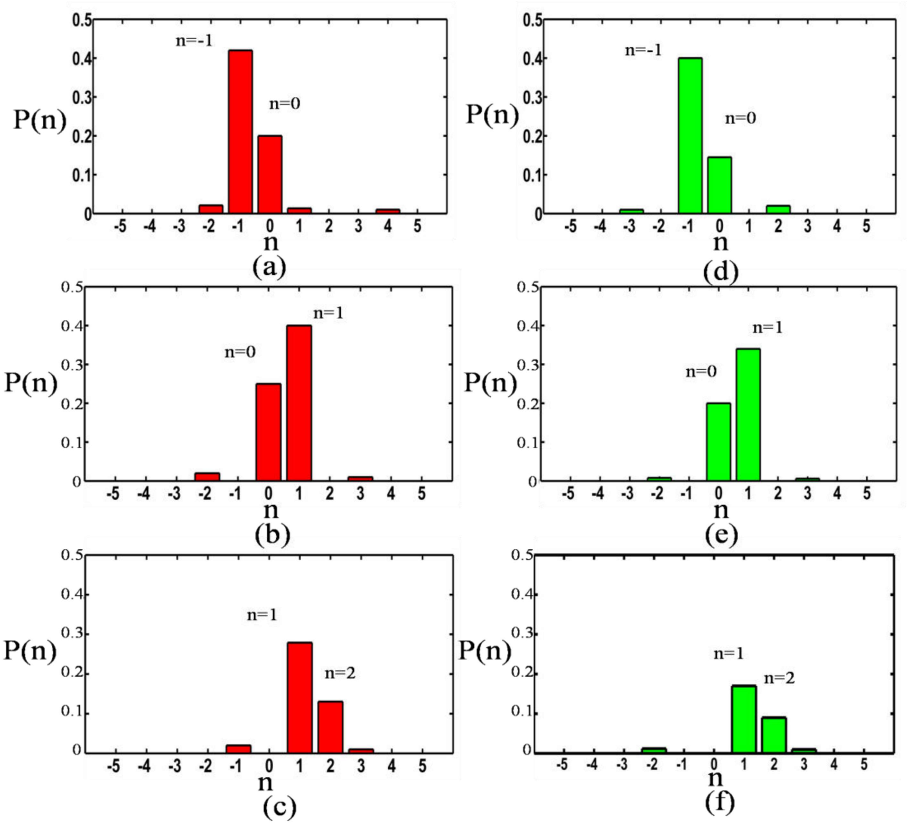

(a) (b) (c) (d) (e) (f)

Fig. 3.8 Panels **(a-c)**, **(d-f)** represent simulation and experimental results of the scattering media for the OAM distribution for three different OAM modes with *l=-0.5, 0.5, and 1.5.*

Simulation and experimental results of the OAM distributions are shown in Fig. 3.8. Figs. 3.8, (a-c) and 3.8, (d-f) represent simulation and experimental results respectively. In Figs. 3.8, (a-c), and (d-f), the red and green color bars reveal the OAM distribution for three different OAM modes with $l = -0.5, 0.5, 1.5$, respectively. Figs. 3.8 (a) and 3.8 (d) show OAM mode with $l = -0.5$ consisting of two integer modes $n = -1, 0$. Figs. 3.8 (b) and 3.8 (e) show OAM mode with $l = 0.5$ consisting of two integer OAM modes $n = 0,1$, and Figs. 3.8 (c) and 3.8 (f) show OAM mode with $l = 1.5$consisting of two integer OAM modes $n = 1, 2$. A small deviation in the experimental and simulated results in Fig. 3.8 is possibly due to the experimental constraints. The fractional vortices in the experiment are generated using the spatial light modulator and the pixelated structure of the SLM may lead to some residual power spectrum of the un-wanted OAM modes

(Nape, 2020). On the other hand, a deviation in the constant cover supports the reference coherence $W_{xx}(\Delta r)$can also influence the reconstruction quality.

3.4 Measuring OAM modes by a three-step phase-shifting in the polarization correlations.

In this technique, we propose a scheme to recover complex OAM modes by measuring limited SPs only with a polarizer. The correlations of the first three SPs (S_0, S_1, S_2) of the random light along with three-step phase-shifting help to restore complex OAM modes. Only the two elements of the matrix help to obtain the real part of the complex Fourier coefficient (CFC). A three-step phase-shifting method (Neil, 2017) is combined with the available Stokes correlation to reduce the number of measurements and retrieve the CPCF. The CPCF provides the complex-valued Fourier coefficient as per the van Cittert-Zernike theorem and helps to extract the incident beam. The incident OAM modes are also probed from the orthogonal helical mode projection of the retrieved CPCF. To avail the benefits of three-step phase-shifting along with the SPs correlations, a phase shift is digitally introduced in the x-polarization state of the incident light. The benefits of our method lie in its ability to recover the complex OAM modes in a completely non-interferometric way, with a lensless geometry. A simulation is performed to verify the proposed method and is confirmed by the experimental tests. The applicability of the proposed method is demonstrated in the recovery of the complex OAM modes in the presence of scattering media. The theoretical investigation, numerical simulation, and experimental demonstration are discussed below.

3.4.1 Theoretical framework

Let us explore the elements $C_{20}(r_1, r_2)$ and $C_{21}(r_1, r_2)$ of the polarization correlation matrix for the recovery of the real part of the CFC and consequently, the composition of OAM modes from the random light. The real part of the CFC is expressed as

$$\begin{aligned} C_{\mathrm{Re}}(r_1, r_2) &= C_{20}(r_1, r_2) + C_{21}(r_1, r_2) \\ &= 4\,\mathrm{Re}\left[\left\{E_x^*(r_1)E_x(r_2)\right\}\left\{E_y^*(r_1)E_x(r_2)\right\}^*\right], \end{aligned} \tag{3.19}$$

Now Eq. (3.19) along with three phase-shifting is used to recover the CFC $C(\Delta r)$ which adduces the information of the compositions of OAM modes. A complex random field in Eq. (3.1) at the observation plane located at any arbitrary distance z is related to the illumination source as follows

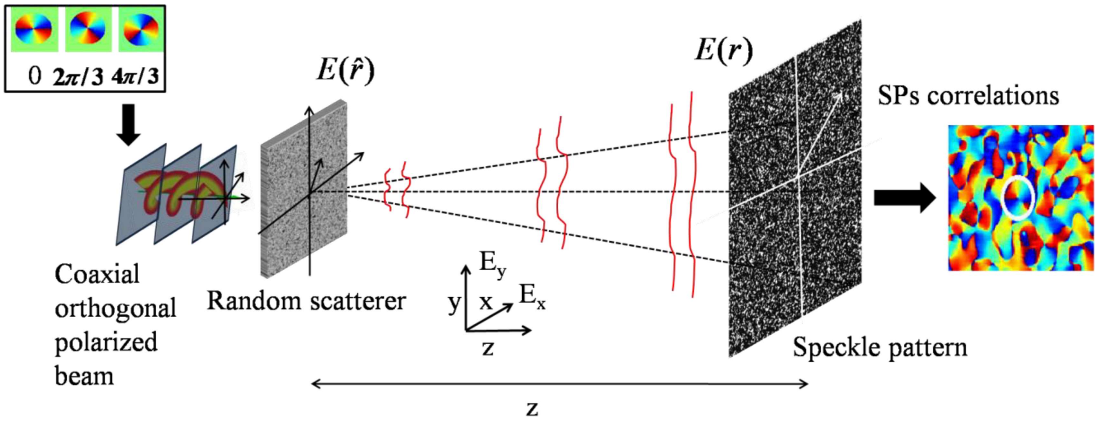

Fig. 3.9 Schematic representation of the three-step phase-shifting technique with SPs correlations.

$$E(r) = \frac{\exp(ikz)}{i\lambda z}\int \exp\left[\frac{ik}{2z}(|r|^2 - 2r.\hat{r}_1 + |\hat{r}_1|^2)\right]E(\hat{r}_1)d\hat{r}_1, \tag{3.20}$$

where $G(r,\hat{r}_1)=\frac{\exp(ikz)}{i\lambda z}\exp\left(ik\frac{|\hat{r}_1|^2+|r|^2-2r.\hat{r}_1}{2z}\right)$ is the Fresnel Kernel. λ denotes the wavelength of the incident beam and $k=\frac{2\pi}{\lambda}$ represents wave number. $\hat{r}$ is the spatial coordinate at the source plane.

Substituting Eq. (3.20) into Eq. (3.19) provides a connection between the CFC and the elements of the CP matrix as follows

$$\left\langle E_a^*(r_1)E_b(r_2)\right\rangle=\left\langle \exp\left(\frac{-ik}{2z}[|r_1|^2-|r_2|^2]\right)\int\int\exp\left(\frac{ik}{2z}[|\hat{r}_2|^2-|\hat{r}_1|^2]\right)E_a^{\;*}(\hat{r}_1)E_b(\hat{r}_2)\right.$$

$$\left.\exp\left(\frac{-ik}{z}\left[(r_2).\hat{r}_2-r_1.\hat{r}_1\right]\right)d\hat{r}_1 d\hat{r}_2\right\rangle, \qquad (3.21)$$

where <.> indicates the ensemble average. The phase curvature outside the integral due to the non-stationary source in Eq. (3.21) is canceled out in the Stokes correlation and helps to achieve a stationary source at any arbitrary plane z as shown in Fig. 3.9. This makes it possible to replace ensemble averaging with spatial averaging and helps to recover the composition of OAM modes from the speckle. Therefore, Eq. (3.21) transforms as

$$\left\langle E_a^*(r_1)E_b(r_2)\right\rangle=\int E_a^*(\hat{r}_1)E_b(\hat{r}_1)\exp\left(-\frac{ik\Delta r.\hat{r}_1}{z}\right)d\hat{r}_1$$

$$=FT\left[E_a^*(\hat{r}_1)E_b(\hat{r}_2)\right], \qquad (3.22)$$

where FT denotes 2D Fourier transform. Eq. (3.22) shows the lensless Fourier transform of the source.

Substituting $E_x(\hat{r}_1) = A_0(\hat{r})\exp(i\psi)$, and $E_y(\hat{r}_1) = A$. where $A_0(\hat{r})$, A represent the amplitude of the incident arbitrary beam and plane wave respectively. Therefore, Eq. (3.22) modifies for x and y polarized beams as

$$\left\langle E_y^*(r_1)E_x(r_2)\right\rangle = FT\left[AA_0(\hat{r})\exp\left(i\psi\right)\right], \tag{3.23}$$

$$\left\langle E_x^*(r_1)E_x(r_2)\right\rangle = FT\left[A_0(\hat{r})A_0(\hat{r})\right], \tag{3.24}$$

Substituting Eq. (3.23) & (3.24) into Eq. (3.19), therefore Eq. (3.19) can be written as

$$C_{\mathrm{Re}}(\Delta r) = 4\,\mathrm{Re}\left[FT\left\{A_0(\hat{r})A_0(\hat{r})\right\}FT\left\{AA_0(\hat{r})\exp(il\psi)\right\}^*\right], \tag{3.25}$$

Now, Eq. (3.25) is considered to build a new theoretical basis to recover CFC from the random light with a three-step phase-shifting strategy. The phase-shifting is digitally acquainted in the incident beam to use the three-step phase-shifting formula (Neil, 1997) as

$$C(\Delta r) = \left(2C_{\mathrm{Re}}^{0}(\Delta r) - C_{\mathrm{Re}}^{2\pi/3}(\Delta r) - C_{\mathrm{Re}}^{4\pi/3}(\Delta r)\right) + \sqrt{3}i\left(C_{\mathrm{Re}}^{2\pi/3}(\Delta r) - C_{\mathrm{Re}}^{4\pi/3}(\Delta r)\right), \tag{3.26}$$

where $C_{\mathrm{Re}}^{0}(\Delta r), C_{\mathrm{Re}}^{2\pi/3}(\Delta r)$, and $C_{\mathrm{Re}}^{4\pi/3}(\Delta r)$ represent the real part of the CPCF of phase shifts of $0, 2\pi/3$, and $4\pi/3$. The CPCF renders the complex-valued Fourier coefficient which provides information of the incident optical beam.

3.4.2 Simulation results

To demonstrate the validity of our technique, we have simulated the different beams with TC *l*=1, 2, -0.5, and 1.5 respectively. Simulation is employed for orthogonally polarized random light fields with wavelength $\lambda = 632.8$ nm. The random fields of the coaxially orthogonal polarization states are generated and modeled by assuming the random phase screens with phase variation with equal probability distribution in the range of $[-\pi,\pi]$. A random field travels from the source to the observation plane at z=200 mm which is modeled using a Fresnel propagation kernel. The Stokes parameters of the random field at the observation plane z=200 mm are calculated from the digitally propagated coherent random fields. These simulated Stokes parameters are used to extract the higher-order Stokes fluctuations correlations as explained in Eq. (3.7) and utilized to estimate the TC of the vortex beam. The elements of the CPCF $C_{20}(\Delta r), C_{21}(\Delta r)$ are obtained by using Eq. (3.7) under the consideration of spatial averaging. Fig. 3.10 shows the simulation results of the helical beams. Figs. 3.10, (a), and (d) indicate the amplitude profile of CPCF and Figs. 3.10, (e-h) indicate the phase profile of CPCF with TC values *l=1, 2* and *n= -0.5, 1.5*, respectively.

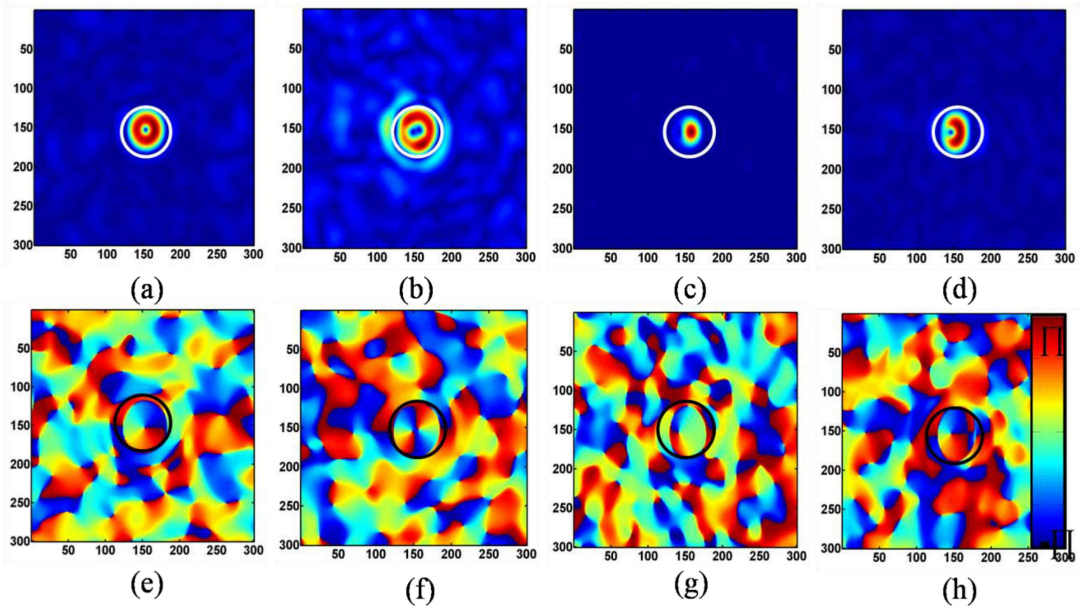

Fig. 3.10 Simulation results: **(a-b), (c-d)** show amplitude distributions of the CPCF for IVB and FOV with TC values *l=1, 2*, and *n=-0.5, 1.5*, respectively. **(e-f), (g-h)** are the corresponding phase distributions.

The amplitude profile of CPCF for the beam with TC values *l=1, 2* show doughnut structure as shown in Figs. 3.10, (a), (b). The dark line in the amplitude profile of CPCF for FOV with TC values $n=-0.5, 1.5$ are depicted in Figs. 3.10, (c), (d). Figs. 3.10, (e), (f), (g), and (h) show the phase profile of CPCF for a beam with TC values $l=1, 2$, and $n=-0.5, 1.5$, respectively.

3.4.3 Experiment and results discussions

To experimentally demonstrate our method, we designed a highly stable non-interferometric experimental geometry for the recovery of complex OAM mode from the complex Fourier coefficients as shown in Fig. 3.11. A detailed description of the experimental method is as follows. A spatially filtered x-polarized light of wavelength 632.8 nm from He-Ne laser incidents on a half-wave plate (HWP) whose fast-axis is at 22.5^0 to diagonally orient the input polarization of the beam. This diagonally polarized coherent beam travels through a 50:50 beam splitter (BS) which splits the incident beam into two identical copies. The transmitted beam from BS propagates towards the reflective type phase-only spatial light modulator (SLM) (Pluto from Holoeye) and illuminates the SLM. The SLM modulates only the x-polarization state of the incident beam and the y-polarization state remains unaffected. In order to generate a vortex beam, the phase profile of different integer vortex beams (IVB) and FOV are displayed on the SLM. The VB is encoded into the x-polarization state while the y-polarization state is reserved as a uniform wave. The beam coming out of the SLM is folded by the BS and propagates through the diffuser (GG). The random scattering from the diffuser scrambles the incident light and creates a granular pattern i.e. speckle. A linear polarizer (LP) is inserted in the path of the random field to characterize the first three SPs of the random light. The first three SPs are evaluated by fixing the transmission axis of the LP to 0^0, $+45^0$, and $+90^0$, respectively. The speckle pattern is captured by a CMOS camera (Model No. DCC3240C; Thor Lab), a resolution of 1280 x 1024 pixels, and a pixel pitch of 5.3 μm, located at a distance of z=200 mm from the diffuser.

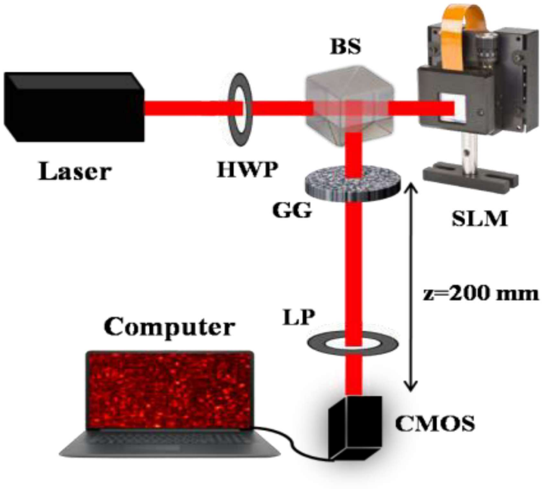

Fig. 3.11 Experimental sketch of the developed technique. He-Ne Laser, BS: beam splitter, HWP: half-wave plate, SLM: spatial light modulator, GG: ground glass, LP: linear polarizer, CMOS: complementary metal-oxide-semiconductor.

A camera records the intensity patterns and the first three SPs are measured from these captured speckle patterns using the following relations (Goldstein, 2017)

$$\begin{aligned} S_0(r) &= I(0^0) + I(90^0), \\ S_1(r) &= I(0^0) - I(90^0), \\ S_2(r) &= 2I(45^0) - S_0(r), \end{aligned} \tag{3.27}$$

where $I(\theta)$ is the intensity at the detector plane and θ is the orientation angle of the polarizer with the x-axis. The correlation of the SPs fluctuations is calculated from the experimentally evaluated SPs as described in Eq. (3.25) and (3.26). The CPCF is retrieved from the measured SPs of the random light which quantitatively recovers the complex amplitude of the Fourier coefficients and hence provides the quantitative information of the VB.

In the experiment, a non-separable state is generated by encoding a spiral and non-spiral wavefront into the two orthogonal polarization states. The phase profiles of the different IVB and FOV are loaded only into one of the polarization states i.e. x and other orthogonal states (y) remain unaffected. The non-separable state of the light co-axially propagates through the random scattering media.

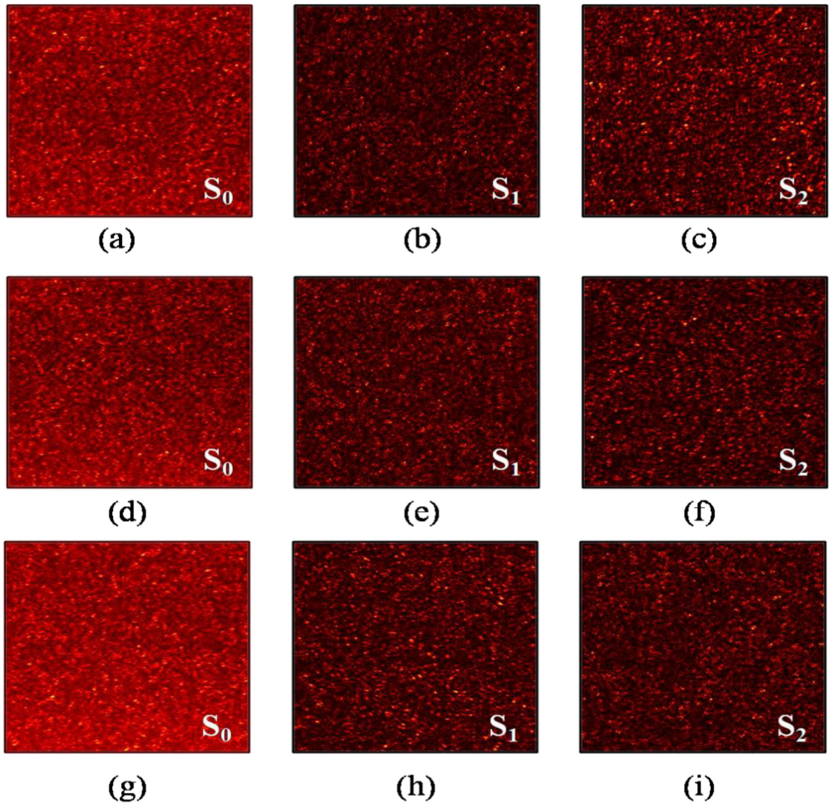

Fig. 3.12 Experimentally measured SPs of the scattered field. **(a-c), (d-f),** and **(g-i)** depict the first three SPs (S_0, S_1, S_2) for VB with $l=1$ with phase shifts of $0, 2\pi/3,$ and $4\pi/3$, respectively.

The first three SPs of the random light measured from the intensity speckle patterns recorded by the camera in the case of the VB with $l=1$ for phase shifts of $0, 2\pi/3,$ and $4\pi/3$ are depicted in Fig. 3.12, (a-i). Figs. 3.12, (d-f), 3.12, (g-i) indicate the first three SPs for $l=1$ with phase shifts of 0, $2\pi/3$ and $4\pi/3$ respectively. The experimental results are depicted in Fig. 3.13. Figs. 3.13, (a-d) indicate the amplitude profile of CPCF and Figs. 3.13, (e-h) indicate the phase profile of CPCF for IVB and FOV with TC values $l=1, 2$ and $n= -0.5, 1.5$, respectively.

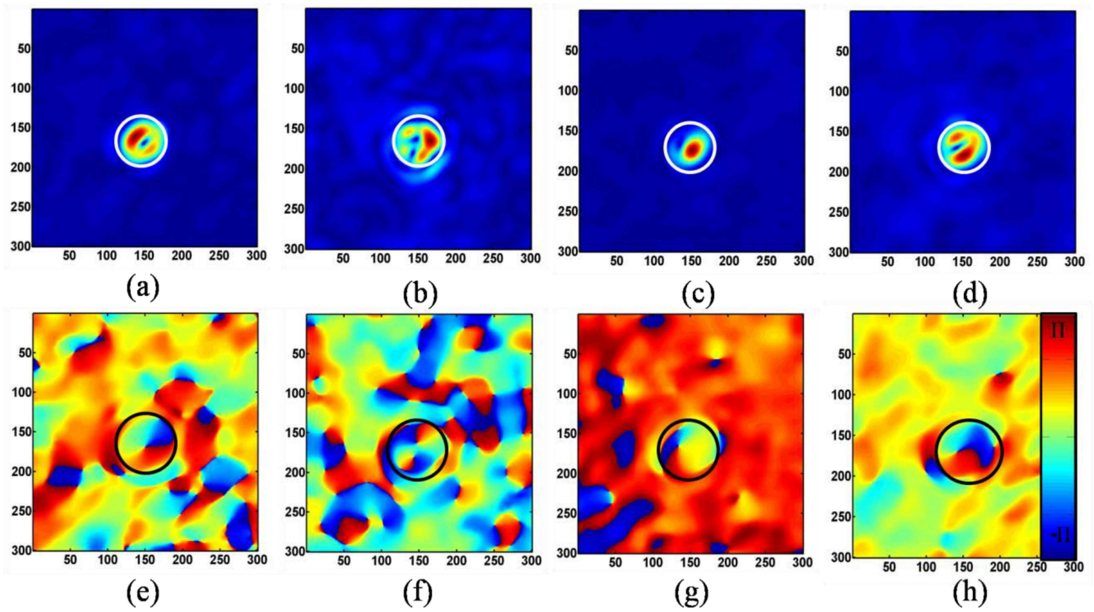

(a) (b) (c) (d)

(e) (f) (g) (h)

Fig. 3.13 Experimental results: **(a-b), (c-d)** show amplitude distributions of CPCF for VB and FOV with TC values *l=1, 2*, and *n=-0.5, 1.5*, respectively. **(e-f), (g-h)** are the corresponding phase distributions.

The amplitude profile of CPCF for IVB with TC values *l=1, 2* show doughnut structure as shown in Figs. 3.13, (a), (b). The dark line in the amplitude profile of CPCF for FOV with TC values *n=-0.5, 1.5* are depicted in Figs. 3.13, (c), (d). Figs. 3.13, (e-h) show the phase profile of CPCF for IVB and FOV with TC values *l=1, 2*, and *n=-0.5, 1.5*, respectively.

3.4.4 OAM spectrum analysis

The OAM mode of the incident VB from the scattered light is also estimated using orthogonal projection of the complex CPCF into the spiral harmonics $\exp(il\varphi)$, where l is the integer value.

Coefficients $A_m(\Delta r)$ are expressed in terms of the angular Fourier transform (Molina-Terriza, 2001) as

$$A_m(\Delta r) = \frac{1}{2\pi}\int_0^{2\pi} d\varphi\, \mathrm{e}^{-il\varphi}\, C(\Delta r), \tag{3.28}$$

The coefficients $A_m(\Delta r)$ are applied to elucidate the OAM distribution of the vortex beam by integrating their squared modulus along with the radial coordinates.

$$P(l) = \frac{1}{S}\int_0^\infty drr\,|A_m(\Delta r)|^2, \tag{3.29}$$

where $S = \sum\int_0^\infty drr\,|A_m(\Delta r)|^2$ represents beam power and $P(l)$ indicates the OAM power spectrum.

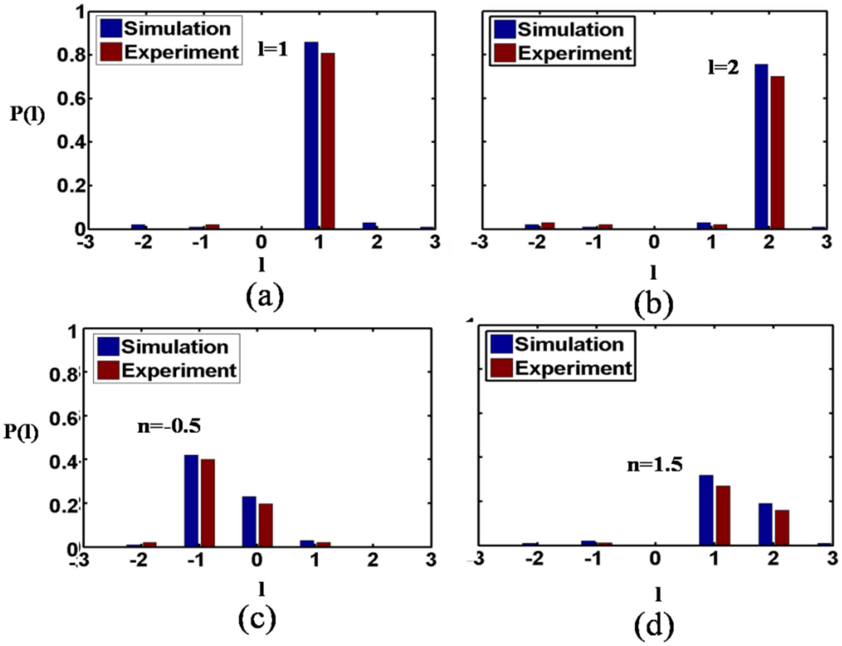

Fig. 3.14 OAM power spectrum: The blue panels in Figs. **(a, b), (c, d)** show OAM simulation results for IVB and FOV with TC values *l=1, 2*, and *n=-0.5, 1.5*. Red panels are the corresponding experimental results.

Simulation and experimental results of the OAM power spectrum are depicted in Fig. 3.14. In Fig. 3.14 the blue color panels show simulation results and the red panels represent the corresponding experimental results. In Figs. 3.14 (a), 3.14 (b), the blue and red color panels show the OAM power spectrum for l=1, 2. Likewise, In Figs. 3.14 (c), 3.14 (d), the blue and red panels represent the OAM power spectrum for two different fractional OAM modes n=-0.5, and 1.5, respectively. Fig. 3.14 (c) shows OAM mode with n=-0.5 is the multiplexing of OAM modes l=-1, 0. Fig. 3.14 (d) indicates that OAM mode with n=1.5 is the multiplexing of OAM modes l=1, 2.

3.5 Conclusion

In this chapter, we have proposed, modeled, and experimentally demonstrated two different quantitative techniques to measure the OAM spectrum of the complex field obscured by random media. The developed theoretical framework is verified by simulation results and also tested by experimental demonstration. The applicability of the developed technique has been demonstrated experimentally to measure the OAM spectrum of the VB and FOV for different cases. The experimental results indicate that the proposed technique shows high flexibility and robustness. These techniques are expected to play a crucial role in optical information processing, sensing, and optical communication.